

Supplementary material: Quantifying early marine diagenesis in shallow-water carbonate sediments

Anne-Sofie C. Ahm^{a,*}, Christian J. Bjerrum^b, Clara L. Blättler^a, Peter K. Swart^c, John A. Higgins^a

^a*Princeton University, Department of Geosciences, Guyot Hall, Princeton, NJ 08544*

^b*University of Copenhagen, Nordic Center for Earth Evolution, Department of Geoscience and Natural Resource Management, Øster Voldgade 10, DK-1350, Copenhagen K*

^c*Department of Marine Geosciences, Rosenstiel School of Marine and Atmospheric Science, University of Miami, 4600 Rickenbacker Causeway, Miami, FL 33149*

1. Geological setting

Carbonate sediments from the Bahamas platform and associated slope provide a modern analog to the carbonate rocks that comprise the ancient geological record. In this study, we used previously published geochemical measurements (Higgins et al., 2018; Blättler et al., 2015) from various sites to constrain and validate a numerical model of carbonate recrystallization, neomorphism, and dolomitization.

The Great Bahamas Bank (GBB) is a modern example of a low-angle prograding carbonate platform and consists almost entirely of a mixture of sediments sourced from the platform top (aragonite) and pelagic sediments from the open ocean (low-Mg calcite) (Swart and Eberli, 2005). The variable abundance of platform and pelagic carbonate have been linked to changes in eustatic sea level with pelagic carbonate dominating during periods of low sea-level and platform exposure (Eberli et al., 1997; Swart and Eberli, 2005; Swart, 2008). These sediments offer the opportunity to study the marine diagenetic alterations associated with large volumes of fluid flow during sea level changes. Detailed descriptions of the geochemistry, sedimentology, and stratigraphy of each site

*Corresponding author

URL: ascahm@gmail.com (Anne-Sofie C. Ahm)

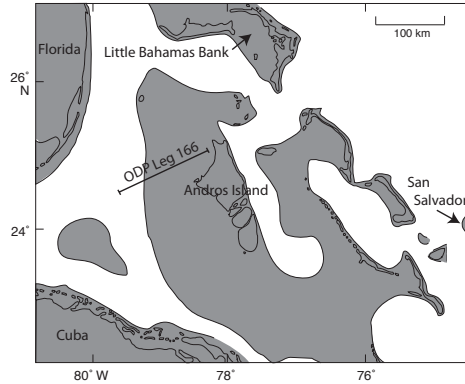


Figure 1: Map of the Bahamas (modified from Eberli et al., 1997) showing the location of ODP Leg 166 (Sites 1003 and 1007), the Little Bahamas Bank (LBB), and San Salvador Island (gray shaded regions are shelf/bank-top environments).

18 from the GBB has been published elsewhere and are only briefly reviewed here
 19 (e.g. Eberli et al., 1997; Ginsburg, 2001; Supko, 1977; Swart and Eberli, 2005;
 20 Swart et al., 1987; Vahrenkamp et al., 1988, 1991).

21 1.1. The Bahamas bank: *Clino* and *Unda*

22 During the initial phase of the Bahamas drilling project, two cores *Clino*
 23 and *Unda* were collected from the shallow platform sediments of the GBB,
 24 west of Andros Island (Eberli et al., 1997; Ginsburg, 2001; Swart and Eberli,
 25 2005). *Unda* is located most proximal to Andros Island, situated 8.5 km east
 26 of *Clino*, and consists of shallow-water platform sands and reefal deposits that
 27 alternate with intervals of deeper skeletal and peloidal platform margin deposits.
 28 Subaerial exposure surfaces and intervals of pervasive dolomitization indicate
 29 that the sediments in *Unda* have seen a wide range of diagenetic conditions.
 30 The samples used in this study are from a ~70 m thick dolomitized interval,
 31 between 350–250 mbsf, containing shallow-water deposits that grade upwards
 32 into skeletal packstone and coral. Pore-fluid profiles indicate that there is a
 33 significant influx of modern seawater throughout the bank top sediments (Swart
 34 et al., 2001).

35 Clino is located at the modern platform margin and is composed of three
 36 major lithologic units: an upper platform section (0–100 mbsf) containing reefal
 37 deposits and several subaerial exposure surfaces, a middle reefal unit with up-
 38 ward progression from deep reef to back reef, and slope sediments (> 200 mbsf)
 39 consisting mainly of monotonous intervals of skeletal and non-skeletal grains.
 40 The mineralogy of the sediments varies widely with depth. The upper part of
 41 the core is dominated by low-Mg calcite (<150 mbsf), whereas between 150–
 42 367 mbsf aragonite is abundant. Below 367 m dolomite is prevalent as a minor
 43 fraction of the sediment. The measurements used in this study are from the
 44 deeper interval below 200 mbsf, below the well studied upper part of the core
 45 that is significantly influenced by meteoric diagenesis (Ginsburg, 2001; Swart
 46 and Eberli, 2005; Swart, 2015). In order to study the isolated dolomitic compo-
 47 nent in the deeper interval, a subset of the $\delta^{44/40}\text{Ca}$ and $\delta^{26}\text{Mg}$ measurements
 48 are from leached samples (Higgins et al., 2018).

49 1.2. ODP Leg 166: Sites 1003 and 1007

50 ODP Leg 166 collected cores from the prograding western margin of the
 51 GBB along a transect from the platform margin into the Straits of Florida
 52 (Eberli et al., 1997). *Site 1003* is located at ~ 483 m water depth on the middle
 53 slope of the western margin, approximately 4 km from the platform edge and
 54 12.6 km from the borehole Clino (Eberli et al., 1997). The core consists of a
 55 ~ 1300 m thick Neogene section with a series of mixed pelagic and bank-derived
 56 carbonate sediments. Sedimentation rates from the lowermost Pleistocene to
 57 the lowermost Miocene seem to be controlled by changes in sea level. The
 58 Pleistocene to upper Pliocene interval is significantly condensed indicating slow
 59 sedimentation rate and decreased input from the bank top. The lower Pliocene
 60 section, on the other hand, is protracted. During this period, the platform
 61 produced a lot of material that was shed onto the upper slope. The early
 62 Miocene section of the core is characterized by pelagic sedimentation rates.
 63 The carbonate mineralogy is dominated by aragonite with lesser amounts of
 64 high-Mg calcite (HMC) and dolomite throughout the upper ~ 100 mbsf. Below

65 this depth, corresponding with the Pliocene/Pleistocene boundary, aragonite
66 decreases markedly, HMC disappears, and low-Mg calcite becomes dominant
67 with a minor dolomitic component (Eberli et al., 1997).

68 *Site 1007* is located on the toe of the slope in 647 m water depth and pen-
69 etrates the entire Neogene and upper Oligocene interval to ~1235 mbsf (Eberli
70 et al., 1997). The sediments alternate between platform-derived material and
71 thinner intervals with pelagic-derived material. The input of pelagic derived
72 material is interpreted to coincide with sea-level lowstands when the platform
73 is exposed. In the upper Pliocene (<200 mbsf), there is an increase in more
74 platform-derived material (highstands) with biowackestone, aragonite needles,
75 and peloids. The Miocene sequences in the deeper part of the core, on the other
76 hand, contain mostly pelagic background sediments and skeletal debris (low-
77 stands). It is likely that the transition from a carbonate ramp in the Miocene
78 to a steep-sided platform in the Pliocene contributed to a turnover from skeletal-
79 to aragonite needle-dominated redeposited sediments (Eberli et al., 1997; Swart
80 and Eberli, 2005).

81 1.3. *Little Bahamas Bank*

82 The Little Bahamas Bank (LBB) is the northernmost carbonate platform
83 of the Bahamian Archipelago and hosts an extensive dolomite body in Neogene
84 sediments at shallow depths (20–100 mbsf). We use measurements from four
85 wells drilled along a N–S transect across Walkers Cay Island (WCI), Sales Cay
86 Island (SCI) and Grand Bahama Island (GB1, GB2) (Vahrenkamp et al., 1988,
87 1991; Williams, 1985). Two main dolomitic units are recognized in these cores:
88 A lower coarse-crystalline Middle Miocene unit and an overlying Pliocene cream-
89 white unit that has been significantly recrystallized. These two dolomitic inter-
90 vals are separated by an unconformity following subaerial exposure (Vahrenkamp
91 et al., 1991). All the measurements presented in this study are from the upper
92 Pliocene dolomite unit between 43–87 mbsf. Previous studies on the petrogra-
93 phy and geochemistry of these dolomites indicate that the dolomitization oc-
94 curred early after sediment deposition by a fluid that was essentially unaltered

95 seawater (Vahrenkamp et al., 1991; Williams, 1985).

96 1.4. *San Salvador Island*

97 A 168 m deep well on the north coast of San Salvador Island consists almost
98 entirely of Neogene dolomites. The dolomites can be subdivided into two dis-
99 tinct types: stratal and massive. The massive dolomites make up most of the
100 core and are largely replacements of supratidal backreef, coralgall and lagoonal
101 facies. The stratal dolomites are thinly bedded and laminated, contain a poor
102 fauna, and have occasional intraclasts and bird's-eye structures (Supko, 1977).
103 The basal rocks in the core are late Miocene in age and show a striking litho-
104 logical similarity with the Miocene strata from LBB (Vahrenkamp et al., 1991).
105 Compared to LBB, however, at least two additional dolomitization episodes have
106 been identified (Swart et al., 1987; Vahrenkamp et al., 1991). Several samples
107 (62 m and 78 m) have Sr isotope ratios close to or even higher than modern day
108 $^{87}\text{Sr}/^{86}\text{Sr}$ (Vahrenkamp et al., 1991; Swart et al., 1987). This Sr isotope signa-
109 ture has been related to eustatic sea-level fluctuations during glaciations, which
110 induced higher isotopic ratios than those of today during parts of the Pleis-
111 tocene. For these dolomites an age of between 100–200 Ka is independently
112 confirmed by U/Th dates (Swart et al., 1987).

113 1.5. *The Monterey Formation*

114 The deep marine Monterey Formation is from the middle Miocene and is
115 exposed along the central Californian coastal area. The hemipelagic to pelagic
116 sediments are rich in organic matter, carbonate, phosphate, and biosilica and
117 act as productive oil source rocks serving the Elwood offshore oil field, a few
118 kilometers off the coast in the Santa Barbara Basin (Bartlett, 1998). All mea-
119 surements used in this study are from drill-core recovered from Platform Holly in
120 the South Elwood oil field (Miller, 1995). Carbonates occur in discrete intervals
121 throughout the core as authigenic beds and nodules formed as early diagenetic
122 concretionary phases prior to sediment compaction (Bramlette, 1946). Carbon-
123 ate precipitation and dolomitization within the sediment was likely driven by

124 remineralization of organic matter through bacterial sulfate reduction, which
 125 would decrease dolomite-inhibiting sulfate and increase carbonate alkalinity in
 126 pore fluids (Compton, 1988). In this study, we explore the limits of the numer-
 127 ical model by simulating authigenic dolomitization in the siliciclastic Monterey
 128 Formation and comparing the results to published geochemical measurements
 129 (Blättler et al., 2015). Two sets of measurements are used: one set is from car-
 130 bonates that have been treated to isolate the dolomite fraction (leached), and
 131 another set is from the bulk carbonate samples (Blättler et al., 2015).

132 2. Analytical methods

133 The majority of the isotopic and elemental measurements used to validate
 134 the model predictions are previously published with thorough descriptions of
 135 the analytical procedures including sample preparation, ion chromatography,
 136 and mass spectrometry (Blättler et al., 2015; Higgins et al., 2018). Additionally,
 137 a subset of new measurements from San Salvador is included in this dataset.
 138 These samples have been analyzed for $\delta^{44/40}\text{Ca}$ values, $\delta^{26}\text{Mg}$ values, and major-
 139 minor elements using identical procedures outlined in Higgins et al. (2018). For
 140 a full description of the methods we refer to Higgins et al. (2018), but here
 141 present a short summary.

142 At Princeton University, samples for isotope analyses were processed us-
 143 ing an automated high-pressure ion chromatography system (IC, Dionex UCS-
 144 5000+) to isolate either Ca or Mg. The purified samples were analyzed for
 145 $\delta^{44/40}\text{Ca}$ and $\delta^{26}\text{Mg}$ on a Thermo Scientific Neptune Plus MC-ICP-MS. Mea-
 146 surements were carried out at low resolution for Mg and medium resolution
 147 for Ca to avoid ArHH^+ interferences. All data are reported in delta notation
 148 relative to a known standard. For Ca isotopes the measured $\delta^{44/42}\text{Ca}$ values
 149 are converted to $\delta^{44/40}\text{Ca}$ values relative to seawater assuming mass dependent
 150 fractionation with a slope of 2.05. Long-term external reproducibility for each
 151 isotopic system is determined based on the difference between two known stan-
 152 dards taken through the full chemical procedure with each batch of samples.

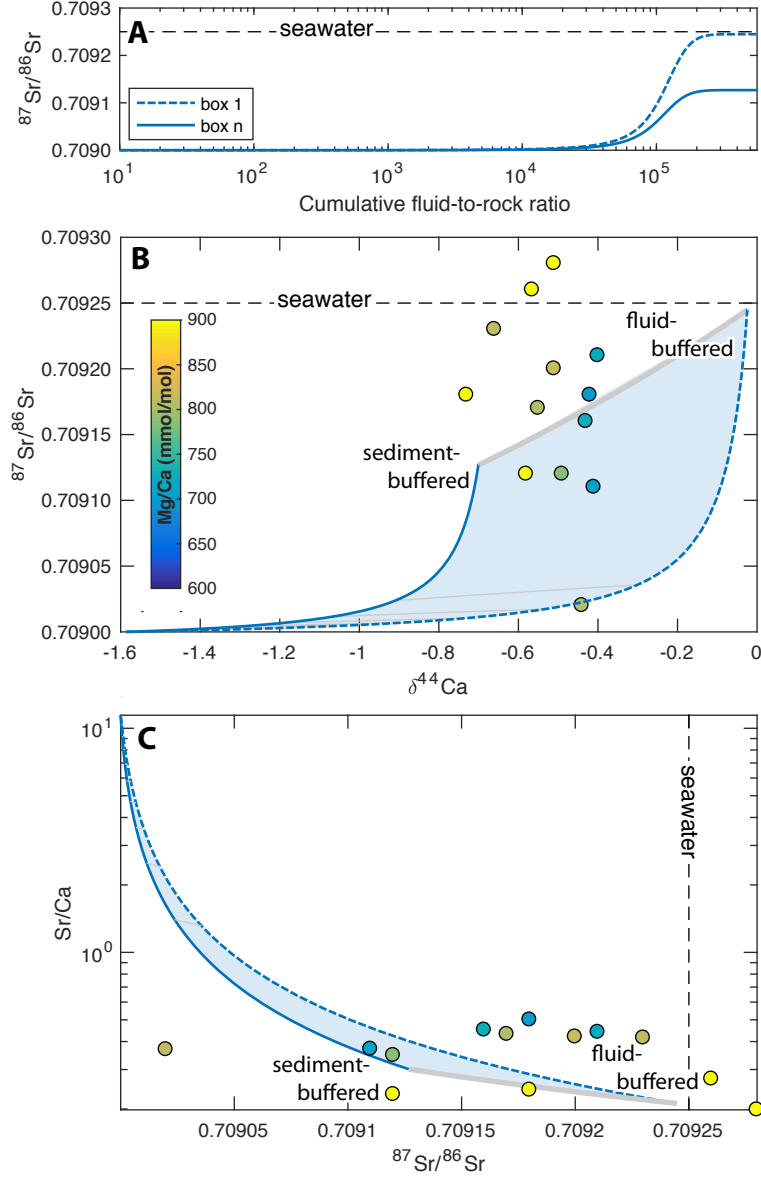


Figure 2: Model results for $^{87}\text{Sr}/^{86}\text{Sr}$ demonstrating dolomitization of primary aragonite ($^{87}\text{Sr}/^{86}\text{Sr}_{\text{primary}} = 0.70900$) in modern seawater (A) Change in composition over time with increasing cumulative fluid-to-rock ratio, (B) Model phase space for $^{87}\text{Sr}/^{86}\text{Sr}$ versus $\delta^{44}/^{40}\text{Ca}$ values from box 1 (fluid-buffered) to box N (sediment-buffered), (C) Model phase space for Sr/Ca versus $^{87}\text{Sr}/^{86}\text{Sr}$ ratios. Samples are $^{87}\text{Sr}/^{86}\text{Sr}$ measurements on dolomites from the San Salvador core (Swart et al., 1987, since we do not have measurements from exact samples, the data has been extrapolated to match our equivalent $\delta^{44}/^{40}\text{Ca}$ and Sr/Ca measurements)

For Ca isotopes the external reproducibility for SRM915b relative to modern seawater is $-1.18 \pm 0.16\text{‰}$ (2σ , $N=125$). $\delta^{44/40}\text{Ca}_{\text{seawater}}$ is $\pm 1.92\text{‰}$ on the SRM-915a scale and $+0.98\text{‰}$ on the bulk silicate bulk Earth scale. For Mg, the long-term external reproducibility of our measurements is estimated by comparing the Mg standard Cambridge-1 and modern seawater against Dead Sea Metal (DSM-3). The measured $\delta^{26}\text{Mg}$ values for Cambridge-1 and seawater are $-2.56 \pm 0.09\text{‰}$ (2σ , $N=76$) and $-0.83 \pm 0.08\text{‰}$ (2σ , $N=99$), respectively.

The Sr/Ca and Mg/Ca ratios were measured on aliquots of dissolved powders analyzed for $\delta^{44/40}\text{Ca}$ and $\delta^{26}\text{Mg}$ isotopes using a ThermoFinnegan Element-2 Inductively Coupled Plasma Mass Spectrometer (ICP-MS). The metal to calcium ratios were determined using a set of matrix-matched in-house standards spanning the sample range. The external reproducibility of the ratios are estimated at $\pm 5 - 7\text{‰}$ from replicate measurements of SRM-88b, a dolomitic limestone.

3. Modeling Sr isotopes

In order to compare model results to the original work of Banner and Hanson (1990), we here include a summary of model predictions for the covariation between $^{87}\text{Sr}/^{86}\text{Sr}$ ratios, $\delta^{44/40}\text{Ca}$ values, and Sr/Ca ratios. Fig. 2 illustrates model cross-plots of $^{87}\text{Sr}/^{86}\text{Sr}$ against both $\delta^{44/40}\text{Ca}$ and Sr/Ca ratios. During dolomitization along a fluid to sediment-buffered trajectory the model predicts linear covariation between $^{87}\text{Sr}/^{86}\text{Sr}$ and $\delta^{44/40}\text{Ca}$ values (grey line, Fig. 2). In addition, due to the high concentrations of Sr in primary aragonite, the bulk sediment remains sediment-buffered with respect to Sr at higher fluid-to-rock ratios than for Ca (i.e. J-curve in Fig. 2B). However, the model results also demonstrate a number of complications for using $^{87}\text{Sr}/^{86}\text{Sr}$ ratios in studying early marine diagenesis: First, recrystallized calcite/dolomite have small concentrations of Sr, which makes the isotopic ratio sensitivity to input from other non-marine sources (e.g. deeper basin fluids or in situ ^{87}Rb decay to ^{87}Sr). For example, dolomite samples from San Salvador have $^{87}\text{Sr}/^{86}\text{Sr}$ ratios that

are more radiogenic than modern seawater (Swart et al., 1987, Fig. 2). Second, the sensitivity to other non-marine sources is further increased by the fact that the range of $^{87}\text{Sr}/^{86}\text{Sr}$ values in modern to late Miocene sediments is small (0.70925–0.70910, DePaolo, 1986). Third, it is highly likely that these sediments have been dolomitized or neomorphosed at different points in time ranging from the Pleistocene to the Miocene (Swart et al., 1987), making it difficult to fit a model trajectory for a single primary end-member $^{87}\text{Sr}/^{86}\text{Sr}$ ratio.

4. Sensitivity test of model parameters

The most important factors governing the modeled isotopic trajectories are: 1) The mineralogy of the primary and diagenetic sediments, 2) the advection and reaction rates, 3) the elemental partitioning, and 4) the mass of the fluid. The model is sensitive to these parameters because they each to some extent influence the abundance of elements in the fluid relative to the sediment along the fluid flow path. In the following section, we test the model sensitivity to changes in these parameters as demonstrated by the shape of the isotopic cross-plot area carved out by the model trajectories. By testing the sensitivity of the model to changes in these boundary conditions, we can isolate the major uncertainties and evaluate their importance and implications for the final predictions.

4.1. Percent alteration

The fraction of diagenetic versus primary minerals in the bulk sediment can be used to infer the percentage (%) of the bulk sediment that has been recrystallized during early diagenesis. The rate of change in the mass of primary minerals is directly proportional to the reaction constant (R) and follows exponential decay:

$$\frac{\partial M_{\text{primary}}}{\partial t} = -R \times M_{\text{primary}} \quad (1)$$

$$M_{\text{primary}}(t) = M_{\text{primary}}(0)e^{-R \times t} \quad (2)$$

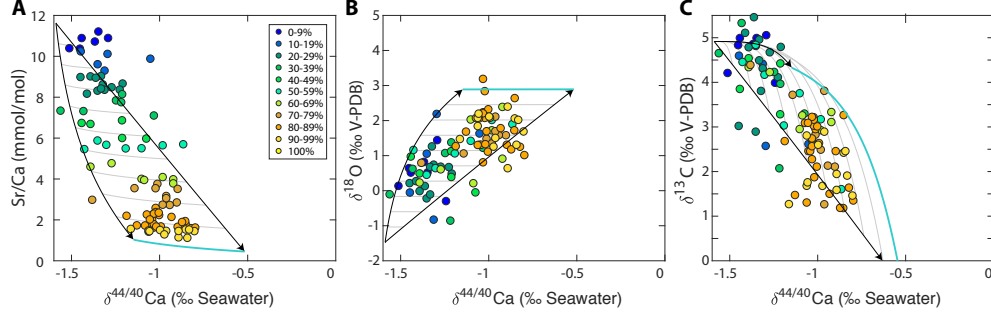


Figure 3: Percentage of the bulk rock that has been diagenetically altered. The modeled trajectories are compared to limestones in the upper part (0–400 mbsf) of core sediments from the Bahamas Transect (Sites 1003, 1007, Clino). The data points are binned into percentages based on correlation between the observed Sr/Ca ratios and the modeled phase space **A** and the binned data are then compared to $\delta^{18}\text{O}$ (**B**), and $\delta^{13}\text{C}$ (**C**) vs. $\delta^{44/40}\text{Ca}$ values

where t is time in years and M_{primary} is the mass of primary minerals.

The model makes specific predictions for each geochemical proxy based on the fraction of primary vs. diagenetic minerals. By comparing the model to limestones from the younger part of the Bahamian dataset (where the initial boundary conditions are best constrained), it is possible to evaluate whether the distribution of data follows the model prediction for percentage alteration across all proxies (Fig. 3). Broadly, the model predictions are in agreement with the measured $\delta^{13}\text{C}$ vs. $\delta^{44/40}\text{Ca}$ values and $\delta^{18}\text{O}$ vs. $\delta^{44/40}\text{Ca}$ values, following a consistent increasing trend from 0 to 100%, although with variable offsets from the specific model trajectories (Fig. 3A-C). This inconsistency is most likely related to variability in the boundary conditions of the Bahamian dataset as the choice of both initial conditions and the specific diagenetic mineral (low-Mg calcite vs. dolomite) will affect the modeled trajectories.

4.2. Mineralogy

The primary mineral. The model is sensitive to mineralogy because the stoichiometry of the bulk sediment directly controls the ratio of elemental abundance in the sediment relative to the fluid. This sediment-fluid ratio (together with the advection/reaction ratio) sets the length scale of the flow path over

Parameter	Baseline	Sensitivity tests	Figure
Length scale (N)	50 m	-	-
α_{Ca}	1.000	-	-
α_{Mg}	0.998	-	-
α_C	1.001	-	-
α_O	1.0330	-	-
K_{Sr}	0.05	0.05 vs. 0.1	Fig. 9
R myr ⁻¹	10%	100% vs. 1%	Fig. 7
u cm/yr	10	100 vs. 1	Fig. 8
Diagenetic mineralogy	dolomite	low-Mg calcite vs. dolomite	Fig. 4
Primary mineralogy	aragonite	low-Mg calcite vs. aragonite	Fig. 5
M_f (Ca ²⁺ mmol/kg)	10.6	106 vs. 1.6	Fig. 10–11
M_f (Mg ²⁺ mmol/kg)	52.8	2.5 vs. 1.3	Fig. 11
δ_f (‰)	$\delta^{44/40}\text{Ca}$: 0‰ $\delta^{26}\text{Mg}$: -0.8‰ $\delta^{13}\text{C}$: -2‰ $\delta^{18}\text{O}$: -29.5‰	-	-

Table 1: Summary and model boundary conditions for each sensitivity test. N is the length scale (i.e. number of boxes), α is the element-specific fractionation factor, K_{Sr} is the partitioning coefficient for Sr, R is the reaction constant, u is advection rate, M_f is the elemental mass in the diagenetic fluid, δ_f is the isotopic composition of the diagenetic fluid. The symbol ‘-’ indicates that the parameter was kept constant in all scenarios. $\delta^{44/40}\text{Ca}$ is stated relative to seawater, $\delta^{26}\text{Mg}$ relative to DSM-3, $\delta^{13}\text{C}$ relative to V-PDB, and $\delta^{18}\text{O}$ relative to V-PDB.

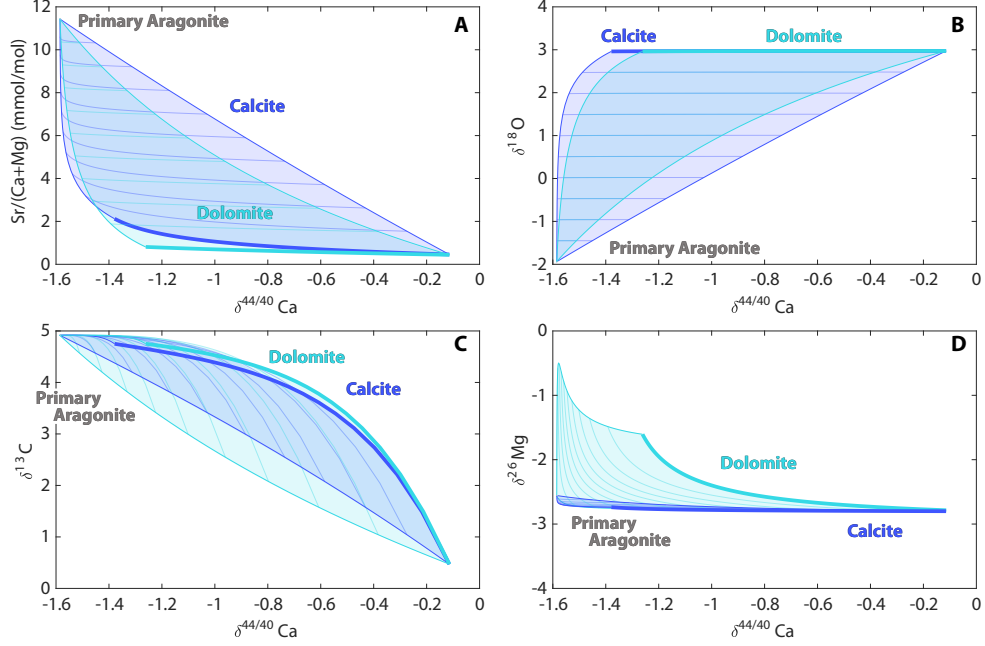


Figure 4: Neomorphism of primary aragonite to low-Mg calcite (dark blue) vs. dolomite (light blue). The model results predict that the shape of the isotopic trajectory from box 1 to N changes based on the mineralogy/stoichiometry of the diagenetic mineral. Here, 50 boxes are included in the model to illustrate the spread of isotopic trajectories from the top to the bottom of the sediment column (box 1– N).

224 which the fluid becomes sediment-buffered. For example, during neomorphism
 225 of aragonite (low concentrations of Mg) the fluid needs to pass through several
 226 boxes (long flow path), dissolving a large volume of sediment, in order to become
 227 sediment buffered with respect to Mg. On the other hand, the dissolution flux
 228 of Mg from high-Mg calcite would be significantly larger and the fluid would
 229 become sediment-buffered over a much smaller length scale (fewer boxes).

230 The concentration of Mg in the primary mineral will also affect the modeled
 231 cross-plot phase space of $\delta^{26}\text{Mg}$ vs. $\delta^{44/40}\text{Ca}$ values. In comparison to calcite
 232 recrystallization, neomorphism of aragonite (with lower concentration of Mg
 233 than calcite) will results in a larger degree of Rayleigh-type distillation of the

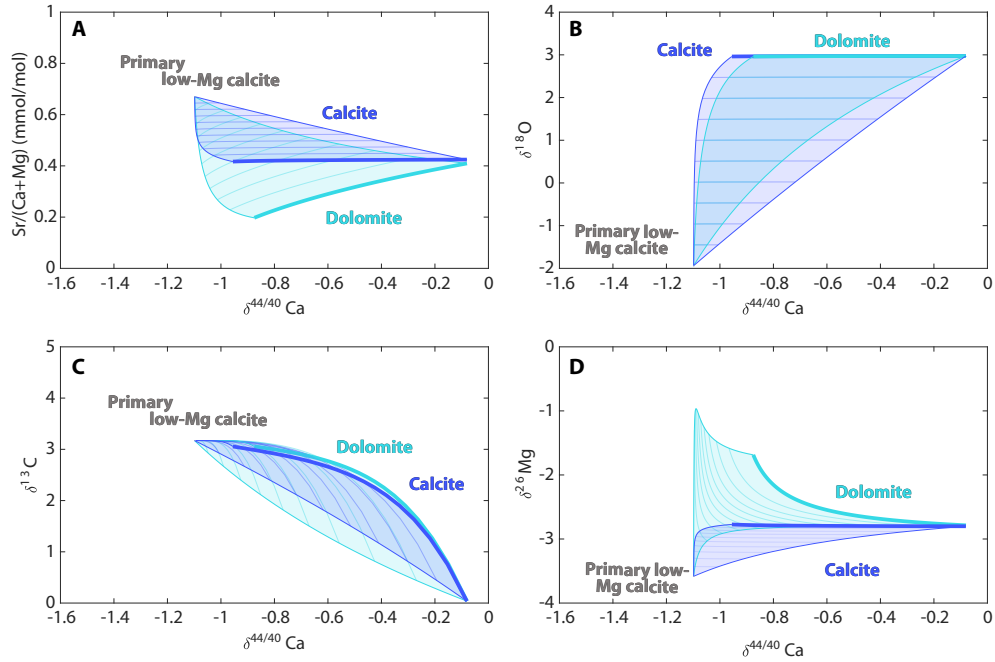


Figure 5: Recrystallization of primary low-Mg calcite (dark blue) vs. dolomitization (light blue). The model results predict that the shape of the isotopic trajectory from box 1 to N changes based on the mineralogy/stoichiometry of the diagenetic mineral (similar to Fig. 4, but with different initial mineralogy)

234 fluid along the flow path, producing more enriched $\delta^{26}\text{Mg}$ values in the sediment-
 235 buffered end-member (Fig. 4–5).

236 Similarly, primary aragonite generally has larger concentrations of Sr than
 237 calcite. The modeled phase-space of Sr/Ca versus $\delta^{44/40}\text{Ca}$ for neomorphism of
 238 aragonite is therefore offset from the modeled phase-space for recrystallization
 239 of calcite (Fig. 4–5). This offset is set by the initial higher Sr/Ca ratios and
 240 depleted $\delta^{44/40}\text{Ca}$ values in primary aragonite relative to calcite (-1.6‰ vs.
 241 -1.1‰ , respectively Blättler et al. 2012; Tang et al. 2008; Gussone et al. 2005).

242 *The diagenetic mineral.* The mineralogy of the diagenetic mineral controls the
 243 partitioning, and thus precipitation rate, of each individual element into the

solid. As the elemental abundance of the pore-fluid is directly related to the precipitation rate, the mineralogy/stoichiometry of the diagenetic mineral also controls the length scale of the flow path over which the fluid becomes sediment-buffered. For example, due to the differences in stoichiometry between diagenetic calcite and dolomite, the concentration of Ca^{2+} in the pore-fluid increases along the flow path during dolomitization while the concentration of Mg^{2+} decreases. In contrast, this phenomenon is not expected during calcite recrystallization or aragonite neomorphism. This process is especially important for the modeled isotopic trajectories of $\delta^{44/40}\text{Ca}$, $\delta^{26}\text{Mg}$, and the concentration of Sr/Ca in the bulk rock (Fig. 6).

The model predicts that for the same set of initial conditions, the incorporation of Sr^{2+} into the diagenetic mineral is lower during dolomitization than during both neomorphism of aragonite or recrystallization of calcite. This difference is due to the increase of Ca^{2+} in the pore-fluids with depth during dolomitization, which blocks the structural sites in the mineral lattice and inhibits Sr incorporation. As a result, for a constant partition coefficient ($K_d = 0.05$), more Sr will be incorporated into low-Mg calcite than dolomite (Fig. 4–5).

The model further predicts that during dolomitization (as opposed to aragonite neomorphism), $\delta^{44/40}\text{Ca}$ values become more enriched in the 100% altered sediment in box *N* (Fig. 6). This difference is controlled by the increase in Ca^{2+} along the flow path during dolomitization leading to Ca^{2+} from infiltrating seawater, with enriched $\delta^{44/40}\text{Ca}$ values, penetrating farther along the flow path.

Dolomitization also differs from aragonite neomorphism in distinctive ways within each individual box. This difference is evident in the modeled cross-plot space of $\delta^{13}\text{C}$ vs. $\delta^{44/40}\text{Ca}$ and $\delta^{18}\text{O}$ vs. $\delta^{44/40}\text{Ca}$ (Fig. 4–5): During aragonite neomorphism, the isotopic trajectory in box 1 (from 0 to 100%) follows a simple linear binary mixing relationship between the primary and diagenetic sediment. In contrast, during dolomitization the concentration of Ca decreases in the bulk sediment over time (from 0 to 100%) and the modeled trajectory in box 1 instead follows a concave mixing pathway.

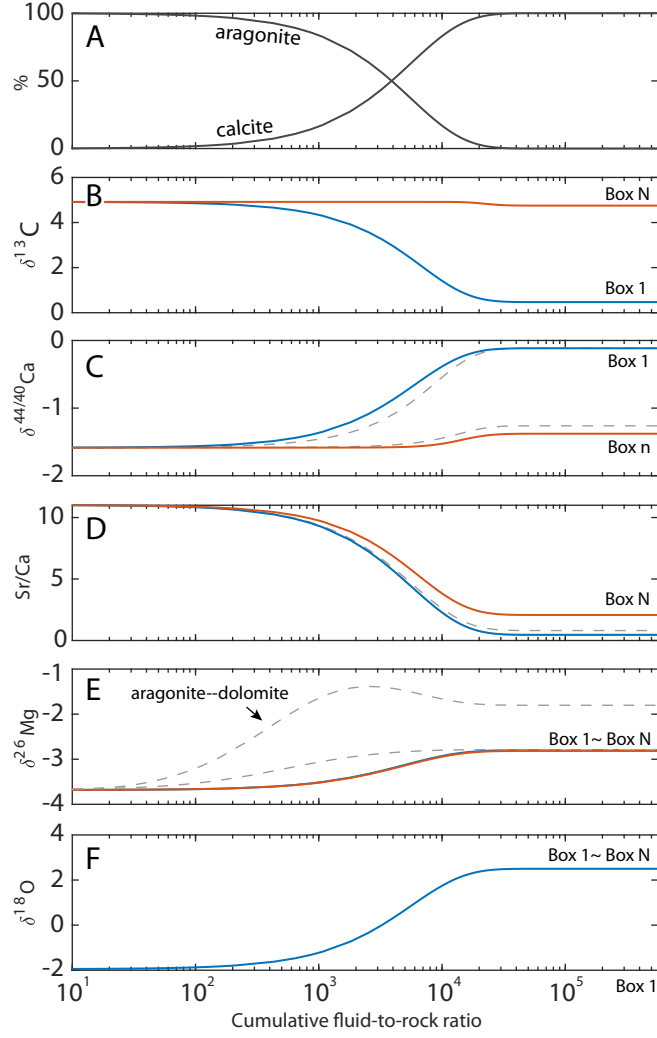


Figure 6: Aragonite neomorphism (**A**) vs. dolomitization (gray dashed line) in box 1 (blue) to box N (red) with increasing cumulative fluid-to-rock ratio over time. The modeled trajectories for $\delta^{13}\text{C}$ values (**B**) and $\delta^{18}\text{O}$ values (**F**) are similar for aragonite neomorphism and dolomitization. The differences in the modeled trajectories for $\delta^{44/40}\text{Ca}$ values (**D**), $\delta^{26}\text{Mg}$ values (**E**), and Sr/Ca ratios (**E**) between aragonite neomorphism and dolomitization is governed by the elemental abundance in the diagenetic mineral as defined by the mineral stoichiometry.

275 The difference between aragonite neomorphism, calcite recrystallization, and
 276 dolomitization is also apparent in the modeled phase space between $\delta^{26}\text{Mg}$ and
 277 $\delta^{44/40}\text{Ca}$ values. The $\delta^{26}\text{Mg}$ values of the bulk sediment are especially sensitive
 278 to the mineralogical difference: Enrichment of ^{26}Mg values due to Rayleigh-type
 279 distillation of the fluid is significantly more pronounced during dolomitization,
 280 whereas recrystallization/neomorphism does not change the downstream pore-
 281 fluid concentration of Mg^{2+} and therefore produces little to no isotopic enrich-
 282 ment (Fig. 4). The modeled cross-plot space of $\delta^{26}\text{Mg}$ vs. $\delta^{44/40}\text{Ca}$ values
 283 illustrates the effect of these differences (Fig. 4–5): the $\delta^{26}\text{Mg}$ values are com-
 284 pletely reset to the original fluid value during calcite recrystallization whereas
 285 $\delta^{26}\text{Mg}$ values are significantly enriched during dolomitization. In both case,
 286 however, the primary $\delta^{26}\text{Mg}$ value of the sediment is completely altered.

287 4.3. Reaction rate

288 The reaction rate (R) imposes a strong control on the length scale of the
 289 flow path over which the fluid becomes sediment-buffered (i.e. over how many
 290 boxes). The model carves out an area in cross-plot space that covers this length
 291 scale from box 1 to box N . Changing the reaction rate will change the isotopic
 292 trajectories (from 0 to 100% recrystallization) in each specific box: Increasing
 293 the reaction rate will drive the pore-fluid towards system more sediment-buffered
 294 conditions over a shorter length scale (fewer boxes). In contrast, decreasing the
 295 reaction rate will drive the pore-fluid towards more fluid-buffered conditions and
 296 a longer length scale of the flow path is needed to reach the sediment-buffered
 297 end-member (Fig. 7). However, independent of the reaction rate, the model
 298 will always converge towards fully sediment-buffered conditions at some point
 299 along an infinitely long flow path (box N). In cross-plot space, the size of the
 300 integrated area from box 1 to box N is thus not dependent on the reaction rate
 301 when the modeled area covers the entire spectrum from fully fluid-buffered to
 302 fully sediment-buffered. The reaction rate remains an important factor when
 303 considering the stratigraphic expression of diagenesis, although the modeled
 304 cross-plot space is unaffected because the number of boxes can be adjusted to

capture the sediment-buffered end-member (Fig. 7). As a result, the model has little capability for constraining diagenetic reaction rates (or advection rates, see below).

4.4. *Advection rate*

The sensitivity of the model to advection rates is similar, though in an opposite sense, to the sensitivity to reaction rates. A 10-fold increase in advection rates produces the same response as a 10-fold decrease in reaction rates and vice versa (Fig. 7-8). Similarly to the sensitivity for reaction rates, the model cross-plot space is unaffected by changing advection rates as long as the length scale/number of boxes is adjusted to capture the entire range from fully fluid-buffered to sediment-buffered conditions. Advection and reaction rates are thus only important for considering the stratigraphic expression of diagenesis. In the model, the main impact of both advection and reaction rates is on the extent to which the top of the sediment column is fully fluid-buffered, since for a low advection/reaction rate ratio, even box 1 will tend to be partially sediment-buffered (Fig. 7-8). This phenomenon can easily be eliminated by adding a re-dissolution flux of the diagenetic minerals to the model, thereby infinitely dissolving the bulk sediment and eventually always reaching the fluid-buffered end-member given enough time.

4.5. *Partition coefficient for strontium*

In the model, the behavior of strontium is entirely determined by its partitioning into various minerals, where strontium generally is partitioned more strongly into the primary mineral than the diagenetic mineral. This behavior leads to an increase in pore-fluid Sr^{2+} along the flow path accompanied by a relative increase in the Sr/Ca ratio of the diagenetic mineral from box 1 to box N . By increasing the partition coefficient (K_d) that prescribes the relationship between the concentration of Sr^{2+} in the pore-fluid and the diagenetic mineral, a larger amount of Sr will be incorporated into the diagenetic mineral for a given pore-fluid concentration (Fig. 9). In contrast, a lower partition coefficient will

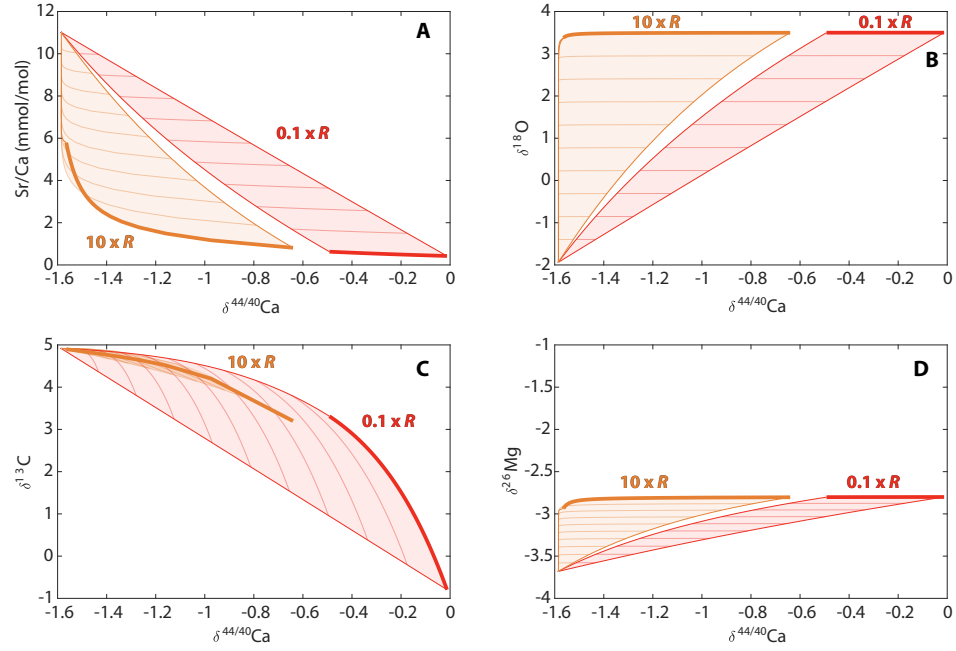


Figure 7: The sensitivity of the model trajectories to changes in reaction rate (R). In the scenario, the model curves out an area in cross-plot space that covers a length scale of 50 m (from box 1 to box 50). Increasing the reaction rate (orange) will drive the pore-fluid system towards more sediment-buffered conditions across all boxes. In contrast, decreasing the reaction rate (red) will drive the pore-fluid system towards more fluid-buffered conditions across all boxes. However, the change in reaction rate can be balanced by changing the length scale of the flow path (i.e. by adding or removing boxes) in order to capture the full range of fluid- to sediment-buffered conditions

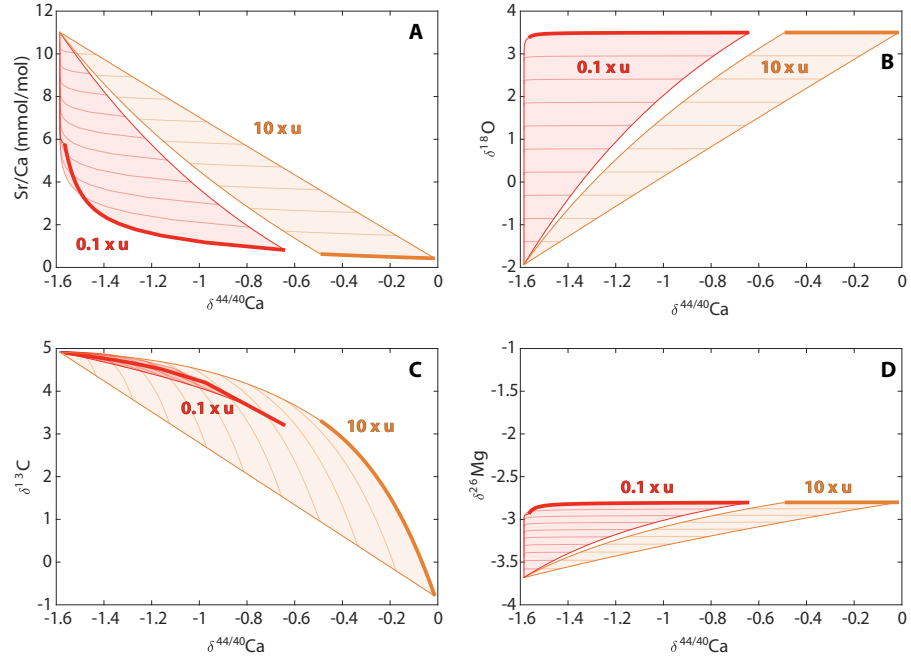


Figure 8: The sensitivity of the model trajectories to changes in advection rate (u). In this scenario, the model carves out an area in cross-plot space that covers a length scale of 50 m (from box 1 to box 50). Increasing the advection rate (orange) will drive the pore-fluid system towards more fluid-buffered conditions whereas, decreasing the reaction rate (red) will drive the pore-fluid system towards more sediment-buffered conditions across all boxes. However, the change in advection rate can be balanced by changing the length scale of the flow path (i.e. by adding or removing boxes) in order to capture the full range of fluid to sediment-buffered conditions (similarly to Fig. 7).

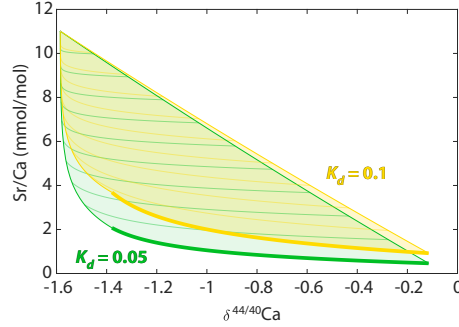


Figure 9: The sensitivity of the model results to the partitioning coefficient of strontium. By increasing the partition coefficient (K_d), a larger amount of Sr will be incorporated into the diagenetic mineral for a similar pore-fluid concentration (yellow). In contrast, a lower partition coefficient will decrease the amount of strontium incorporated into the diagenetic mineral across all boxes (box 1–50, green).

334 decrease the amount of Sr incorporated into the diagenetic mineral (Fig. 9).
 335 In addition to the empirically defined partition coefficient and the Sr^{2+} concen-
 336 tration of the fluid, the incorporation of strontium into the diagenetic mineral
 337 is also affected by the concentration of Ca^{2+} in the fluid. A higher concentra-
 338 tion of Ca^{2+} in the fluid will decrease the partitioning of strontium into the
 339 diagenetic mineral phases, as Ca^{2+} blocks the available structural sites in the
 340 mineral lattice. This behavior is demonstrated when modeling dolomitization
 341 where pore-fluid Ca^{2+} increases along the flow path (Fig. 4).

342 4.6. Fluid composition

343 The concentration of various elements in the fluid – a direct lever on the
 344 relative mass ratio between fluid and solid – has a strong control on the shape
 345 of the modeled isotopic trajectories. For example, the concentration of Ca^{2+} in
 346 the fluid controls the degree to which $\delta^{44/40}\text{Ca}$ values are reset and covary with
 347 other proxies during diagenesis. High Ca^{2+} concentrations in the infiltrating
 348 fluid will result in pore-fluids that are more fluid-buffered over a greater length
 349 scale. As a result, bulk sediment $\delta^{44/40}\text{Ca}$ values will be more reset towards the

350 initial fluid value across all 50 boxes (Fig. 10). In contrast, a lower concentration
 351 of Ca^{2+} in the initial diagenetic fluid will result in pore-fluids that are more
 352 sediment-buffered, and bulk sediment $\delta^{44/40}\text{Ca}$ values will be less reset across a
 353 similar length scale (Fig. 10) .

354 The model demonstrates that the relative concentrations of solutes in the
 355 pore-fluid has a direct effect on the area carved out by the model in cross-plot
 356 space. For example, relatively higher Ca^{2+} concentrations in the diagenetic
 357 fluid will shift the covariation between $\delta^{13}\text{C}$ and $\delta^{44/40}\text{Ca}$ in the bulk sediment
 358 towards generally heavier $\delta^{44/40}\text{Ca}$ values over a similar range in $\delta^{13}\text{C}$ (Fig.
 359 10). Similarly, the covariation between $\delta^{26}\text{Mg}$ vs. $\delta^{44/40}\text{Ca}$ values in the bulk
 360 sediment changes depending on the relative concentrations of Ca^{2+} and Mg^{2+}
 361 in the fluid (Fig. 11): During dolomitization, the model predicts that a higher
 362 initial Ca^{2+} concentration in the fluid will increase the slope of the isotopic
 363 trajectory (100% recrystallization from box 1- N), reflecting the more enriched
 364 $\delta^{44/40}\text{Ca}$ values of the diagenetic fluid (i.e. more influence from seawater). Low-
 365 ering the Mg^{2+} concentration in the fluid will produce a similar response in the
 366 modeled trajectories because $\delta^{26}\text{Mg}$ will be less sensitive to resetting relative
 367 to $\delta^{44/40}\text{Ca}$ (Fig. 11). As a result, modern seawater (which contains higher
 368 concentrations of Mg^{2+} than Ca^{2+}) will produce a concave and less steep fluid-
 369 to sediment-buffered isotopic trajectory between $\delta^{26}\text{Mg}$ and $\delta^{44/40}\text{Ca}$ from box
 370 1- N . In contrast, the model results predict that lower seawater $\text{Mg}^{2+}/\text{Ca}^{2+}$ ra-
 371 tios will produce an increase in the slope between $\delta^{26}\text{Mg}$ and $\delta^{44/40}\text{Ca}$ values
 372 of the diagenetic sediment during early marine diagenesis (Fig. 11). Due to
 373 distillation of the fluid during dolomitization, the slope of this modeled trajec-
 374 tory can never become positive as $\delta^{26}\text{Mg}$ always will be more enriched in box N
 375 than box 1. However, the model predicts that during aragonite neomorphism,
 376 a tipping point exists at very low fluid Mg/Ca ratios ($\sim < 0.02$) where $\delta^{44/40}\text{Ca}$
 377 values of the bulk sediment become more sensitive to diagenesis than $\delta^{26}\text{Mg}$.
 378 As a result, the $\delta^{44/40}\text{Ca}$ values are reset before (lower box number) the $\delta^{26}\text{Mg}$
 379 values thereby producing and inverted isotopic trajectory (Fig. 11).

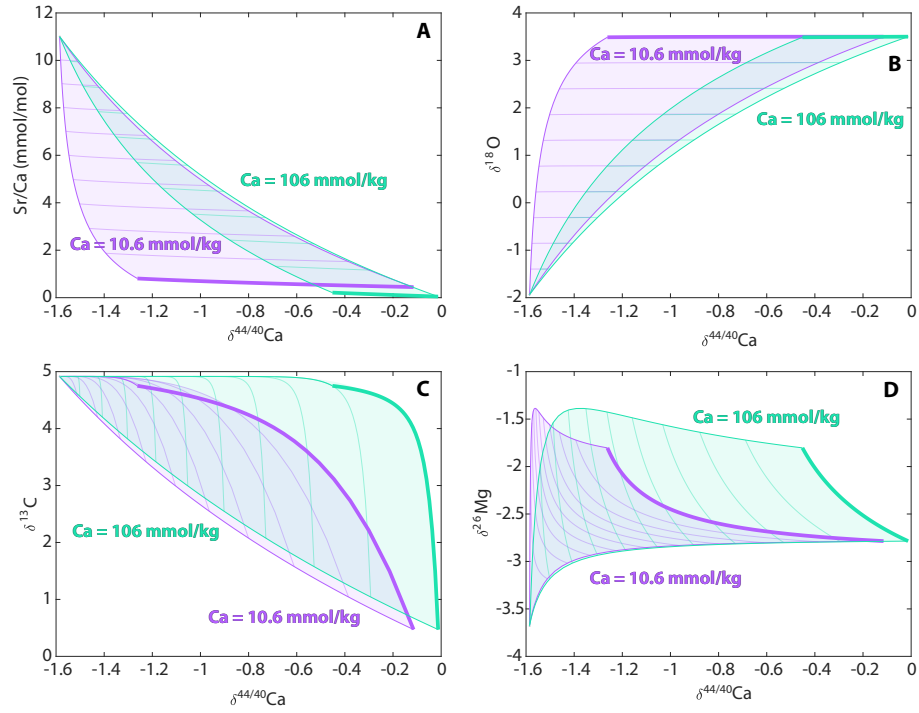


Figure 10: Model sensitivity to Ca^{2+} concentrations in the infiltrating fluid. For a higher Ca^{2+} concentration (orange) the pore-fluids are more fluid-buffered over a greater length scale. For a lower Ca^{2+} concentration (purple) the pore-fluids are more sediment-buffered and bulk sediment $\delta^{44/40}\text{Ca}$ values will be less reset across a similar length scale.

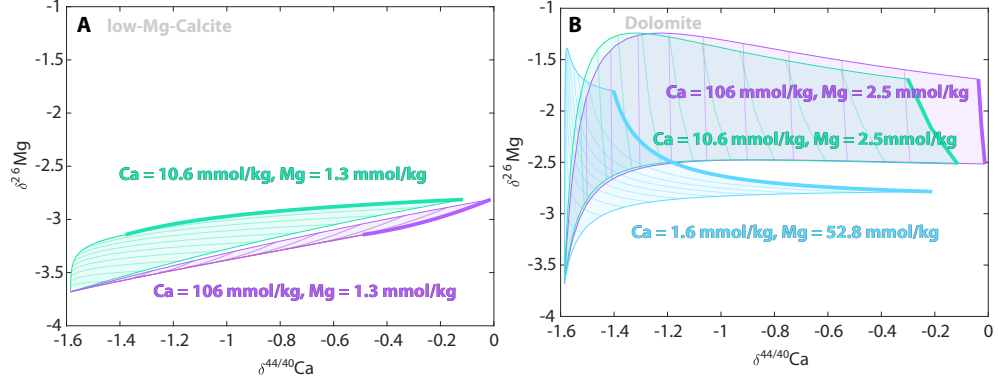


Figure 11: Model sensitivity to the concentration of Ca^{2+} and Mg^{2+} in the infiltrating fluid. The covariation between $\delta^{26}\text{Mg}$ and $\delta^{44/40}\text{Ca}$ values in the diagenetic sediment (diagenetic end-member indicated by thicker line) is directly determined by the Mg/Ca ratio of the diagenetic fluid. **A.** During aragonite neomorphism, a tipping point exists at very low fluid Mg/Ca ratios where $\delta^{44/40}\text{Ca}$ values of the bulk sediment become more sensitive to diagenetic alteration than $\delta^{26}\text{Mg}$ values. **B.** In contrast, due to distillation of the fluid during dolomitization, the slope of the $\delta^{26}\text{Mg}$ vs. $\delta^{44/40}\text{Ca}$ modeled trajectory can never become positive as $\delta^{26}\text{Mg}$ are always more enriched in box N than box 1 and as $\delta^{44/40}\text{Ca}$ values are always more enriched in box 1 than box N .

380 5. $\delta^{18}\text{O}$ values in bulk sediment from the Bahamas

381 The isotopic fractionation between $\delta^{18}\text{O}$ values in carbonate minerals and
 382 pore-fluids can be used as a proxy for temperature during diagenesis (e.g. Böhm
 383 et al., 2000; Kim and O’Neil, 1997). The sensitivity of $\delta^{18}\text{O}$ value to temperature
 384 is reflected in the limestones from the deeper part of the Bahamian cores (400–
 385 1200 mbsf), where sediments are recrystallized during later burial diagenesis
 386 (Murray and Swart, 2017; Swart and Eberli, 2005; Swart, 2015). Pore-fluids in
 387 these older sediments are sediment-buffered with respect to carbon and calcium,
 388 but in response to the higher temperatures at depth, the $\delta^{18}\text{O}$ values of the bulk
 389 sediment decrease (from +2 to -2‰). If assuming no change in fluid $\delta^{18}\text{O}$ values
 390 with depth, the observed change in $\delta^{18}\text{O}$ values can be estimated to reflect an
 391 increase in temperature from 10 to 30°C (Kim and O’Neil, 1997). This estimate
 392 broadly agrees with calculations of the local geothermal gradient in a well north

393 of Andros Island ($\sim 1.3^\circ\text{C}$ per 100 m; Epstein and Clark 2009).

394 Oxygen isotopes are also sensitivity to early marine diagenesis. In cores
395 from the Bahamas Transect, aragonite neomorphism is indirectly reflected in
396 progressively increasing $\delta^{18}\text{O}$ values with depth (from 0–400 mbsf): Primary
397 aragonite that precipitates in warm surface waters ($\sim 27^\circ\text{C}$) is isotopically de-
398 pleted (-1.5‰), while diagenetic low-Mg calcite that precipitates in the cooler
399 deeper waters on the slope ($\sim 10^\circ\text{C}$, Eberli et al. 1997) is isotopically enriched
400 ($+3\text{‰}$). The stratigraphic trend in $\delta^{18}\text{O}$ values from 0 to 400 mbsf thus broadly
401 reflects increasing mixing between primary aragonite and diagenetic calcite with
402 depth (see Fig. 5 main text). However, the temperature difference between sur-
403 face and deeper water masses cannot solely explain the measured range in $\delta^{18}\text{O}$
404 values from the Bahamas Transect (using estimates of α from Böhm et al., 2000;
405 Kim and O’Neil, 1997), suggesting that the deeper water masses and/or pore-
406 fluids are isotopically enriched in comparison with surface waters masses (-30.5
407 vs. -29‰ V-PDB, respectively, equivalent to $-0.5\text{--}1\text{‰}$ SMOW, Coplen et al.
408 1983).

409 Pore-fluid profiles from across the Bahamas demonstrate that $\delta^{18}\text{O}$ values
410 generally increase with depth (Swart et al., 2000; Kramer et al., 2000; Murray
411 and Swart, 2017; Winkelstern and Lohmann, 2016). These isotopically enriched
412 fluids may be remnants of Pleistocene seawater from the last glacial period
413 (Adkins and Schrag, 2003; Schrag et al., 1996) or they may reflect mixing be-
414 tween reflux brines and normal seawater (Murray and Swart, 2017). Swart et al.
415 (2000) attributed the pore-water $\delta^{18}\text{O}$ profile to carbonate recrystallization dur-
416 ing burial where the dissolution of aragonite ($\delta^{18}\text{O}$ -enriched) and the subsequent
417 precipitation of calcite at higher temperature ($\delta^{18}\text{O}$ -depleted) would drive an
418 increase in pore-water $\delta^{18}\text{O}$ values with depth. However, our model cannot re-
419 produce the observed trends in pore-fluid chemistry, suggesting that this type
420 of enrichment of fluid $\delta^{18}\text{O}$ values can only occur during extreme closed-system
421 conditions that require high reaction rates in combination with very little fluid
422 flow: For example, using reaction rates of 10% per Ma, flow rates of 0.5 cm/yr,
423 and a fractionation factor of 1.0289 yields an enrichment of 0.09‰ in pore-fluid

424 $\delta^{18}\text{O}$ values along a 50 m flow path.

425 References

- 426 Adkins J.F., Schrag D.P., 2003. Reconstructing last glacial maximum bottom
427 water salinities from deep-sea sediment pore fluid profiles. *Earth Planet. Sci.*
428 *Lett.* **216**, 109–123. doi:10.1016/S0012-821X(03)00502-8.
- 429 Banner J.L., Hanson G.N., 1990. Calculation of simultaneous isotopic and trace
430 element variations during water-rock interaction with applications to carbon-
431 ate diagenesis. *Geochim. Cosmochim. Acta* **54**, 3123–3137. doi:10.1016/
432 0016-7037(90)90128-8.
- 433 Bartlett W.L., 1998. Elwood Oil Field Santa Barbar County, California. *AAPG*
434 *Structure and Petroleum Geology* Oil and Gas Fields Section, 217–237. URL:
- 435 Blättler C.L., Henderson G.M., Jenkyns H.C., 2012. Explaining the Phanerozoic
436 Ca isotope history of seawater. *Geology* **40**, 843–846. doi:10.1130/g33191.1.
- 437 Blättler C.L., Miller N.R., Higgins J.A., 2015. Mg and Ca isotope signatures of
438 authigenic dolomite in siliceous deep-sea sediments. *Earth Planet. Sci. Lett.*
439 **419**, 32–42. doi:10.1016/j.epsl.2015.03.006.
- 440 Böhm F., Joachimski M.M., Dullo W.C., Eisenhauer A., Lehnert H., Reitner
441 J., Wörheide, G., 2000. Oxygen isotope fractionation in marine aragonite
442 of coralline sponges. *Geochim. et Cosmochim. Acta* **64**, 1695–1703. doi:10.
443 1016/S0016-7037(99)00408-1.
- 444 Bramlette M.N., 1946. The Monterey Formation of California and the Origin
445 of Its Siliceous Rocks.. volume **212** of *Geological Survey Professional Paper*.
446 US Government Printing Office.
- 447 Compton J.S., 1988. Degree of supersaturation and precipitation of organogenic
448 dolomite. *Geology* **16**, 318–321.

- 449 Coplen T.B., Kendall C., Hopple J., 1983. Comparison of stable isotope refer-
450 ence samples. *Nature* **302**, 236–238.
- 451 DePaolo D.J., 1986. Detailed record of the Neogene Sr isotopic evolution of
452 seawater from DSDP Site 590B. *Geology* **14**, 103–106.
- 453 Eberli G.P., Swart P.K., Malone M.J., 1997. Shipboard Scientific Party: College
454 Station, TX (Ocean Drilling Program). *Proc. ODP Init. Reports* **166**. doi:10.
455 2973/odp.proc.ir.166.1997.
- 456 Epstein S.A., Clark D., 2009. Hydrocarbon potential of the Mesozoic carbon-
457 ates of the Bahamas. *Carbonates and Evaporites* **24**, 97–138. doi:10.1007/
458 BF03182088.
- 459 Ginsburg R.N., 2001. Subsurface Geology of a Prograding Carbonate Plat-
460 form Margin, Great Bahama Bank: Results of the Bahamas Drilling Project.
461 *SEPM Society for Sedimentary Geology*. **70** doi:10.2110/pec.01.70.
- 462 Gussone N., Böhm F., Eisenhauer A., Dietzel M., Heuser A., Teichert B.M.A.,
463 Reitner J., Wörheide G., Dullo W.C., 2005. Calcium isotope fractionation in
464 calcite and aragonite. *Geochim. et Cosmochim. Acta* **69**, 4485–4494. doi:10.
465 1016/j.gca.2005.06.003.
- 466 Higgins J.A., Blättler C.L., Lundstrom E.A., Santiago-Ramos D., Akhtar A.,
467 Ahm A-S.C., Bialik O., Holmden C., Bradbury H., Murray S.T., Swart P.,
468 2018. Mineralogy, early marine diagenesis, and the chemistry of shallow water
469 carbonate sediments. *Geochim. et Cosmochim. Acta*. **220**, 512–534. doi:10.
470 1016/j.gca.2017.09.046.
- 471 Kim S.T., O’Neil J.R., 1997. Equilibrium and nonequilibrium oxygen isotope
472 effects in synthetic carbonates. *Geochim. et Cosmochim. Acta* **61**, 3461–3475.
473 doi:10.1016/S0016-7037(97)00169-5.
- 474 Kramer P.A., Swart P.K., De Carlo E.H., Schovsbo N.H., 2000. Overview of
475 interstitial fluid and sediment geochemistry, Site 1003-1007 (Bahamas Tran-

476 sect). *Proc. Ocean Drill. Prog. Sci. Results* **166**, 179–195. doi:10.2973/odp.
477 *proc.sr.166.117.2000*.

478 Miller N.R., 1995. Lithostratigraphic signal evaluation of the Miocene Monterey
479 Formation, South Elwood Field, Santa Barbara-Ventura Basin, California.
480 Ph.D. thesis. University of Texas at Dallas. Richardson, TX, United States.

481 Murray S.T., Swart P.K., 2017. Evaluating formation fluid models and cali-
482 brations using clumped isotope paleothermometry on Bahamian dolomites.
483 *Geochim. et Cosmochim. Acta* **206**, 73–93. doi:10.1016/j.gca.2017.02.
484 021.

485 Schrag D.P., Hampt G., Murray D.W., 1996. Pore fluid constraints on the
486 temperature and oxygen isotopic composition of the glacial ocean. *Science*
487 **272**, 1930–1932. doi:10.1126/science.272.5270.1930,

488 Supko P.R., 1977. Subsurface dolomites, San Salvador, Bahamas. *J. Sediment.*
489 *Res.* **47**, 1063–1077. doi:10.1306/212F72DE-2B24-11D7-8648000102C1865D.

490 Swart P.K., 2008. Global synchronous changes in the carbon isotopic composi-
491 tion of carbonate sediments unrelated to changes in the global carbon cycle.
492 *Proc. Natl. Acad. Sci.* **105**, 13741–13745. doi:10.1073/pnas.0802841105.

493 Swart P.K., 2015. The geochemistry of carbonate diagenesis: The past, present
494 and future. *Sedimentology* **62**, 1233–1304. doi:10.1111/sed.12205.

495 Swart P.K., Eberli G., 2005. The nature of the $\delta^{13}\text{C}$ of periplatform sediments:
496 Implications for stratigraphy and the global carbon cycle. *Sediment. Geol.*
497 **175**, 115–129. doi:10.1016/j.sedgeo.2004.12.029.

498 Swart P.K., Eberli G.P., Malone M.J., Sarg, J.F., 2000. The oxygen isotopic
499 composition of interstitial waters: evidence for fluid flow and recrystallization
500 in the margin of Great Bahama Bank. *Proc. ODP, Sci. Results*, 166 doi:10.
501 2973/odp.proc.sr.166.130.2000.

- 502 Swart P.K., Elderfield H., Ostlund G., 2001. The geochemistry of pore fluids
503 from bore holes in the Great Bahamas Bank. *SEPM Special Publication* **70**,
504 163–173.
- 505 Swart P.K., Ruiz J., Holmes C.W., 1987. Use of strontium isotopes to con-
506 strain the timing and mode of dolomitization of upper Cenozoic sediments
507 in a core from San Salvador, Bahamas. *Geology* **15**, 262–265. doi:10.1130/
508 0091-7613(1987)15<262:uositc>2.0.co;2.
- 509 Tang J., Dietzel M., Böhm F., Köhler S.J., Eisenhauer A., 2008. $\text{Sr}^{2+}/\text{Ca}^{2+}$ and
510 $^{44}\text{Ca}/^{40}\text{Ca}$ fractionation during inorganic calcite formation: II. Ca isotopes.
511 *Geochim. et Cosmochim. Acta* **72**, 3733–3745. doi:10.1016/j.gca.2008.05.
512 033.
- 513 Vahrenkamp V.C., Swart P.K., Ruiz J., 1988. Constraints and interpretation
514 of $^{87}\text{Sr}/^{86}\text{Sr}$ ratios in Cenozoic dolomites. *Geophys. Res. Lett.* **15**, 385–388.
515 doi:10.1029/GL015i004p00385.
- 516 Vahrenkamp V.C., Swart P.K., Ruiz J., 1991. Episodic dolomitiza-
517 tion of late Cenozoic carbonates in the Bahamas; evidence from stron-
518 tium isotopes. *J. Sediment. Res.* **61**, 1002–1014. doi:10.1306/
519 d4267825-2b26-11d7-8648000102c1865d.
- 520 Williams S.C., 1985. Stratigraphy, facies evolution, and diagenesis of late Ceno-
521 zoic limestones and dolomites, Little Bahamas Bank, bahamas (molluscan,
522 Neotectonics, Biostratography). Dissertations from ProQuest **1493**.
- 523 Winkelstern I.Z., Lohmann K.C., 2016. Shallow burial alteration of dolomite and
524 limestone clumped isotope geochemistry. *Geology* doi:10.1130/g37809.1.